Regional Impact of Snow-Darkening on Snow Pack and the Atmosphere During a Severe Saharan Dust Deposition Event in Eurasia

Anika Rohde[1], Heike Vogel[1], Gholam Ali Hoshyaripour[1], Christoph Kottmeier[1], and Bernhard Vogel[1]

[1]Institute of Meteorology and Climate Research, Karlsruhe Institute of Technology (KIT), Karlsruhe, Germany

Abstract Light-absorbing impurities such as mineral dust can play a major role in reducing the albedo of snow surfaces. Particularly in spring, deposited dust particles lead to increased snow melt and trigger further feedbacks at the land surface and in the atmosphere. Quantifying the extent of dust-induced variations is difficult due to high variability in the spatial distribution of mineral dust and snow. We present an extension of a fully coupled atmospheric and land surface model system to address the impact of mineral dust on the snow albedo across Eurasia. We evaluated the short-term effects of Saharan dust in a case study. To obtain robust results, we performed an ensemble simulation followed by statistical analysis. Mountainous regions showed a strong impact of dust deposition on snow depth. We found a mean significant reduction of -1.4 cm in the Caucasus Mountains after 1 week. However, areas with flat terrain near the snow line also showed strong effects despite lower dust concentrations. Here, the feedback to dust deposition was more pronounced as increase in surface temperature and air temperature. In the region surrounding the snow line, we found an average significant surface warming of 0.9 K after 1 week. This study shows that the impact of mineral dust deposition depends on several factors. Primarily, these are altitude, slope, snow depth, and snow cover fraction. Especially in complex terrain, it is therefore necessary to use fully coupled models to investigate the effects of mineral dust on snow pack and the atmosphere.

Plain Language Summary Dust particles such as Saharan dust can darken snow surfaces, leading to increased absorption of solar radiation. The result is earlier snow melt in the spring and a warming of the land surface. Predicting dust deposition and subsequent regional impacts is difficult because the distribution of snow and dust appears in complex patterns depending on the landscape. We extended an atmospheric and land surface model system to investigate the impact of Saharan dust particles across Eurasia during a Saharan dust transport event. We found that mountainous regions are particularly affected by the dust particles, leading to increased snowmelt. In addition, regions with thin and patchy snow cover show a strong response to the dust particles, mainly causing a warming of the land surface. We found that the effects of dust particles depend on different regional characteristics. Therefore, when investigating dust on snow, it is important to use model systems that represent both the atmospheric process and surface properties properly.

1. Introduction

Snow-covered surfaces are characterized by a high capacity to reflect solar radiation. In the visible spectrum, the albedo of pure snow is roughly 96–99% (Wiscombe & Warren, 1980). The current knowledge about the properties of snow albedo was well summarized by Skiles and Painter (2018). The major factors that determine the optical properties of snow are the snow micro-structure, snow depth, and the content of impurities. The latter has only recently become the focus of attention.

A model for computing snow albedo with influences of light-absorbing impurities (LAI) was presented by Warren and Wiscombe (1980). But at first, only simplistic studies were conducted with climate models where the albedo was systematically changed (e.g., Hansen, 2005; Hansen & Nazarenko, 2004; Jacobson, 2004). This was followed by measurements (e.g., Aoki et al., 2006; Meinander et al., 2013; Peltoniemi et al., 2015; Svensson et al., 2016) and more advanced simulations involving sophisticated snow or meteorological models and aerosol properties (e.g., Di Mauro et al., 2019; Donth et al., 2020; Dumont et al., 2014, 2020; Flanner & Zender, 2005; Flanner et al., 2009; Rahimi et al., 2020; Sarangi et al., 2019, 2020; Tuzet et al., 2017, 2019; Usha et al., 2020). The most frequently discussed aerosol is black carbon (BC). Due to the dark color, it has the strongest impact

Visualization: Anika Rohde
Writing – original draft: Anika Rohde,
Heike Vogel, Gholam Ali Hoshyaripour,
Bernhard Vogel
Writing – review & editing: Anika
Rohde, Heike Vogel, Gholam Ali
Hoshyaripour, Bernhard Vogel

on the snow properties (e.g., Nagorski et al., 2019; Rahimi et al., 2020; Sarangi et al., 2020). However, several studies showed that mineral dust transported to several regions (e.g., central Asia mountains, Colorado in the US) outweighs BC because of its large abundance (Gautam et al., 2013; Kaspari et al., 2014; Painter et al., 2010; Svensson et al., 2018; Yasunari et al., 2015). Furthermore, Sarangi et al. (2020) demonstrated that the impact of dust can increase with altitude relative to the impact of BC. Snow with aerosol contamination melts out earlier in spring time (Bryant et al., 2013; Deems et al., 2013; Fujita, 2007; Painter et al., 2010; Skiles et al., 2015).

The sophisticated snow model SNOWPACK (Bartelt & Lehning, 2002; Lehning et al., 1999; Lehning, Bartelt, Brown, & Fierz, 2002; Lehning, Bartelt, Brown, Fierz, & Satyawali, 2002) coupled with SNow, ICe, and Aerosol Radiation (SNICAR, Flanner & Zender, 2005) and the sophisticated snow model Crocus (Brun et al., 1992; Vionnet et al., 2012) allow precise studies of the energetic processes in a snow pack and the radiative impact of LAI in snow. For instance, Dumont et al. (2020) used Crocus to investigate the impact of aerosols on snow melting during a major Saharan dust deposition event in the Russian Caucasus Mountains. They found that depending on dust concentration, snow layer height, and altitude, the snow melt out advanced between 12 and 30 days. Snow model studies alone, however, do not provide information about the spatial variability, the influence of the terrain, and moreover, they are not able to capture feedback processes with the atmosphere. The coupling of such a complex snow model with an atmospheric model is at least in operational application not feasible because of the immensely high computational costs.

There are several studies based on climate models that deal with the long-term influence of LAI. With regard to Eurasia, the study by Lau et al. (2018) identifies regions that show particularly strong influence using the NASA GEOS-5 (National Aeronautics and Space Administration Goddard Earth Observing System, Version 5) climate model. They found an annual mean increase in surface skin temperature most pronounced in Western Eurasia, East Asia, and the Tibetan Plateau. The reduction in snow mass and the increase in shortwave radiation coincided with these regions. Climate models help us to identify overall trends but are not suitable to investigate individual events in more detail and to compare results with observations on weather scale.

Weather models with high temporal and spatial resolution can help us to better understand the immediate effects and feedback mechanisms of LAI on various meteorological variables. These include the studies such as Qian et al. (2009) and Rahimi et al. (2020) both employing the WRF-Chem model (Weather Research and Forecasting - Chemistry). One major finding of Qian et al. (2009) was that about half of the decrease in landscape-scale albedo is attributed to the vanishing of snow cover and revealing the dark ground below (snow-albedo feedback). Rahimi et al. (2020) coupled SNICAR to the WRF-Chem model, which covers LAI impact on snow albedo based on snow grain size and the theory of Wiscombe and Warren (1980). SNICAR considers Mie parameters for snow in only one visible and four near-infrared bands. However, the spectral snow albedo is highly variable and highly sensitive to impurities, especially in the visible range (e.g., Skiles & Painter, 2018; Warren & Wiscombe, 1980). Rahimi et al. (2020) found a general increase in 2 m temperature by 0.15 K in the Rocky Mountains (United States) and an earlier snow melt out of 4 days due to BC and dust. They found a 2% reduction in snow albedo at high altitudes.

Weather models have high sensitivity to small perturbation. Due to the nonlinearities in the fundamental equations, these small perturbations can result in nonperiodic small-scale fluctuations. Rahimi et al. (2020) observed such anomalies in snow water equivalent and temperature feedback, which they referred to as a probable result of internal model variability. Due to limited computational resources, it was not possible for them to investigate these fluctuations further, and they recommended the application of ensemble simulations to investigate the LAI effect. As far as we know, there are no such elaborate ensemble studies on LAIs that assessed direct correlations between different atmospheric and land surface variables.

We extended the model system ICOsahedral Nonhydrostatic atmosphere and climate with Aerosols and Reactive Trace gases (ICON-ART) by a parametrization of a spectral snow albedo which considers snow aging processes and the darkening effect of mineral dust on snow in 18 wavelength bands. As a result, we obtained a framework featuring an atmospheric and land model system that allows the online computation of the impact of mineral dust on snow and the associated feedback of the land surface and the atmosphere. For the first time, the effects of mineral dust on snow have been simulated with high spectral resolution in an extensive ensemble simulation setup. This setup allows statistically robust results on short-term effects of mineral dust on snow.

The impact of Saharan dust was investigated in a simulation covering Europe and western parts of Asia. In spring 2018, a particularly impactful dust event occurred (Barkan & Alpert, 2020; Dumont et al., 2020; Marmureanu et al., 2019; Monteiro et al., 2022; Solomos et al., 2018). We investigated this event using the fully coupled model

system ICON-ART to disentangle regional influences and drivers on the snow-darkening effect. The goal was to assess the spatial and temporal distribution of the mineral dust during this event and quantify the resulting feedback. The questions that we addressed in this study are as follows: (a) Did the distribution of mineral dust result in the formation of particularly vulnerable regions? (b) How intense were the feedbacks in the land surface and the atmosphere during the severe dust event? (c) Which surface and atmospheric variables were most strongly affected during this event. The paper is organized as follows: in Section 2 we explain the methodology and assumption, which is followed by the results and discussions in Section 3. We summarize the results and provide the conclusions in Section 4.

2. Methodology

2.1. ICON-ART Model System

The ICON model is a weather and climate model that solves the full three-dimensional non-hydrostatic and compressible Navier-Stokes equations (Giorgetta et al., 2018; Zängl et al., 2015). The equations are discretized on an unstructured triangular grid that is based on a spherical icosahedron. This feature allows the model to operate at various scales and be refined seamlessly. The results of a global simulation run can be used to drive an ICON simulation in the regional configuration Limited Area Mode (LAM). In this study, the radiation in ICON is treated by the RRTM (Rapid Radiative Transfer Model) described by Mlawer et al. (1997). This radiative transfer model calculates shortwave and longwave radiation in 30 spectral bands between 0.2 and 1,000 μm.

At the lower boundary of the atmosphere, ICON is coupled with the land surface and vegetation model TERRA_ML. The land surface model serves as a transmitter of heat, moisture, and momentum between the atmospheric component and the land surface (Doms et al., 2018). Interactions include, for example, surface roughness length, vegetation-dependent evaporation, vertical heat, water transport in the soil, photosynthetic active radiation, surface albedo, and snow cover. TERRA_ML provides two different snow models. The first is used in operational weather forecast and is a single-layer snow model. As pointed out by previous studies (e.g., Jacobi et al., 2015), a single-layer snow model scheme is not capable to adequately represent the energy budget and the temperature profile in a snow pack. It has been found that such schemes are inferior in describing the evolution of the snowpack and some hydrological processes compared to snow schemes with multiple layers (e.g., Zsoter et al., 2022). Furthermore, the ability to create an aerosol stratification, which describes the vertical distribution of the aerosols in snow, is not possible when having only one single layer. As pointed out by Skiles and Painter (2019), the resurfacing of the aerosols plays a major role in the optical properties of the snow. These are the main aspects why in this study an experimental snow model is used that was developed at German weather service (DWD) (Machulskaya & Lykosov, 2008). It is also incorporated in the TERRA_ML surface scheme with adjustable number of snow layers. The application of multiple snow layers allows for vertical profiles of snow temperature, water content, and snow density.

ART is a sub-module of ICON that enables the simulation of aerosols, trace gases, and related feedbacks (Rieger et al., 2015; Schröter et al., 2018). It can treat various aerosol types including sea salt, volcanic ash, mineral dust, and several gaseous tracers. The DWD provides daily ICON-ART mineral dust forecasts, which are available for comparison with the results of other forecasting systems through the Sand and Dust Storm Warning Advisory and Assessment System (WMO Barcelona Dust Regional Center, 2021). Model results are validated daily by the DWD. A detailed description of the treatment of aerosol processes can be found in Rieger et al. (2015); Schröter et al. (2018). In this work, we use the two-moment aerosol description. The mineral dust is represented in three log-normal modes. The optical properties of dust in ART are extinction coefficient, single-scattering albedo, and asymmetry parameter (Gasch et al., 2017; Rieger et al., 2017). The dust emission is calculated online based on soil type, soil moisture content and wind speed. The parametrization is based on Vogel et al. (2006) and accounts for emission due to saltation. Mineral dust can leave the atmosphere via sedimentation, dry, and wet deposition. When the aerosols are removed from the atmosphere, they reach the land surface. We add these aerosols to the snow cover, if such is present. The particles are finally removed from the system as soon as the snow cover disappears.

2.2. Dust and Snow Interaction

In order to study the radiative interactions between snow and mineral dust, we implemented a spectral snow albedo parametrization that considers the age of the snow, the influence of dust deposition, ground effects and the distinction between direct and indirect radiation. Here, we provide a brief summary of the individual processes that are necessary for the computation. A more detailed description of the model implementations is available in
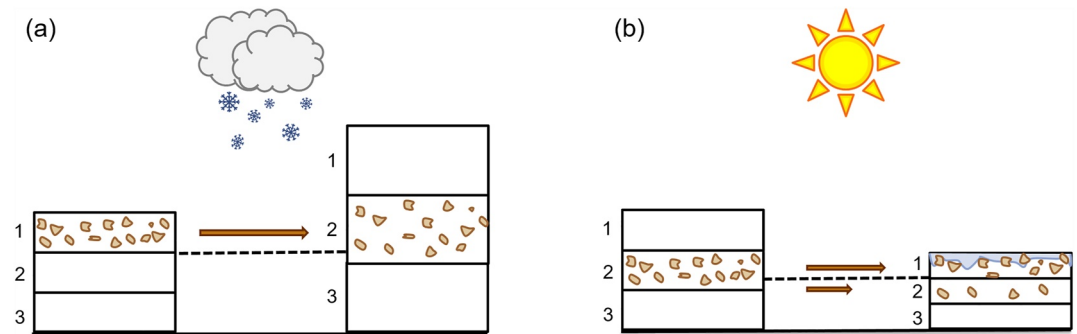
Figure 1. Conceptual diagram of aerosol mass transfer between snow layers during (a) snow accumulation and (b) snow melt.

Rohde (2021). The complete collection of snow albedo equations is described in Wiscombe and Warren (1980) and Warren and Wiscombe (1980).

In order to determine the optically active dust layer at the surface, we added layering processes of aerosols in the snow model. We assume that dust particles remain in the snow layer, in which they are deposited and can be covered by new snowfall. We introduced tracking of mineral dust by linking the dust mass to the height of the respective snow layer above the ground. We consider the mineral dust mass to be uniformly distributed within a snow layer. A shifting of the position of the aerosols is only taking place when the total snow depth changes. Regarding this, snowfall, compression and other physical processes are ignored in this approach. We assume that both snow melt and accumulation of snow occur at the upper boundary toward the atmosphere. Figure 1 illustrates the transfer of dust mass between snow layers during snow accumulation and snow melt.

Regarding the optical properties of snow, we introduced a new prognostic variable, the optical equivalent snow grain radius, into the experimental snow model. This includes the growth of snow grains (aging process) based on the equation of Essery et al. (2001). However, we extended the aging factors for additional temperature ranges, which were validated in Jäkel et al. (2021). Furthermore, the influence of rain was added, which accelerates the aging of snow. We incorporated the Mie coefficients of snow grains with a radius ranging between 20 and 2,500 μm and a wavelength range of 0.30–1.65 μm. The basis is the refractive indices from the collection of Warren and Brandt (2008). We implemented the spectral snow albedo based on these Mie coefficients and the theories of Wiscombe and Warren (1980) into the model.

The interaction of the optical properties of mineral dust and snow is considered at the top 10 cm of the snow pack, adjoining the atmosphere. According to Warren and Wiscombe (1980), the modification of the snow albedo due to aerosols is carried out by weighted averaging of the extinction cross sections and scatter cross sections using the total cross sections as weighing factors. With our new developments, this weighing is computed online in the simulation in a total of 18 wavelength bands (11 visible, 7 near infrared). The advantage of multiple bands in the visible range is that specific wavelength bands can be affected depending on the absorption characteristics of the specific aerosol. Since the absorption of radiation by snow increases rapidly toward the near infrared, the influence of different bands has different strengths. In the final step, the snow albedo is spectrally integrated to obtain snow albedo in the visible and the near infrared bands.

Our computations assume an external mixing of spherical snow grains and spherical mineral dust particles. Dang et al. (2016) found out that the albedo of nonspherical snow grains is slightly higher. However, they state that the albedo of nonspherical snow grains can be mimicked by simply using smaller grains with spherical shape. It needs to be pointed out that the external mixing between dust and snow is mostly apparent when dust deposits under dry conditions. In the case of wet deposition, internal mixing occurs. A couple of studies investigated the snow-darkening effect of internally mixed aerosols in snow and found out that the darkening is further enhanced due to internal mixing (Flanner et al., 2012; Shi et al., 2021).

2.3. Model Configuration

We performed a global simulation of a dust event at a grid spacing of about 40 km (R2B06). The simulation covered the time period from 22 March 2018, 0 UTC to 1 April 2018, 0 UTC (10 days). At the start of the
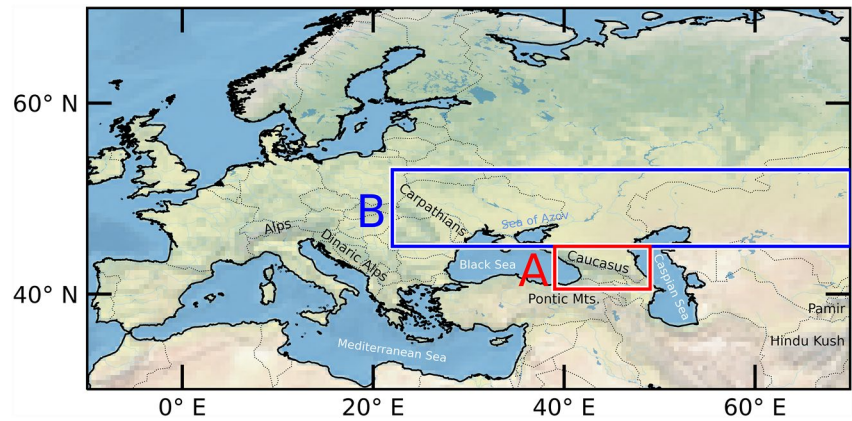
Figure 2. ICOsahedral Nonhydrostatic atmosphere and climate with Aerosols and Reactive Trace gases Limited Area Mode domain with outlines of region A including the Caucasus Mountains and region B containing the moving snow line during spring time melt in March 2018.

simulation, the model was initialized using two different sources. The meteorological state was initialized using ECMWF - IFS (European Centre for Medium-Range Weather Forecasts - Integrated Forecasting System) data from 22 March 2018, 0 UTC. The mineral dust data were obtained from the operational dust forecast using ICON-ART performed by the DWD.

The simulation was a free run without reinitialization throughout the 10 days. Due to the fact that both the deposition and the snow cover are strongly dependent on the terrain and that they are spatially highly variable, the resolution of 40 km was further increased. For this purpose, we applied the ICON-ART LAM with the grid spacing of 10 km (R2B08) during the same time period. The hourly results of the meteorological variables as well as the mineral dust of the global R2B06 simulation were used to force the LAM domain. The investigation area extends over large parts of the snow-covered areas of Europe and Asia between 30°–70°N and 10°W–70°E.

Figure 2 shows the study region of the ICON-ART LAM domain and the two smaller regions where certain processes are investigated in more detail. Region A covers the Caucasus Mountains, where a severe dust deposition event was reported (Barkan & Alpert, 2020; Dumont et al., 2020). It covers the area between 40.5°–45°N and 39°–49°E. Region B covers the snow line which moves toward the north due to spring melting processes. Here, the term does not refer to the snow line, which indicates the lower limit of the snow cap at high terrain. Instead, the term "snow line" refers to the ever-changing equatorward limit of the snow cover. This snow line migrates due to seasonal changes. In cold seasons, this boundary lies further south, and in warm seasons, it lies in northerly territories. Region B extends over the area between 45°–53°N and 22°–70°E. The ongoing melting during springtime makes the snow especially receptive for the influence of aerosol particles (Skiles & Painter, 2019). According to Lau et al. (2018), this is one of the main vulnerable regions to aerosol deposition on the Eurasian continent.

To investigate the influence of mineral dust on snow surfaces, two sets of experiments were executed in parallel. The reference experiment (REF) contains all new implementations concerning the spectral snow albedo, but excludes the interaction of the optical properties of mineral dust and snow. In other words, the mineral dust is present in the reference experiment but does not affect the snow albedo. It is assumed that the snow is clean. We performed a second experiment with the same setup as the reference experiment, but the interaction of the optical properties of dust and snow is included. This corresponds to the snow-darkening simulation (SDS).

Rahimi et al. (2020) highlighted that a large variability prevails at higher resolution caused by internal model variability. To achieve a more robust result, we performed an ensemble simulation. The application of ensemble simulations is a well-established method for the identification of result uncertainties. This tool is used in particular in numerical weather prediction, where short time periods are computed at high resolution. For the analysis, we consider the arithmetic mean over all individual simulation results. We generated the members via a stochastic perturbation of model internal physical parameters within their uncertainty range. The same perturbation was introduced pairwise in one REF and one SDS simulation, which allows for a comparison of the experiments. In this way, 40 pairs were generated and a total of 80 simulations. The influence of mineral dust is determined

by the arithmetic mean over all individual differences between the respective simulation pairs (SDS−REF). All variables refer only to cells in which at least one ensemble member, either SDS or REF, contains snow. Other cells that are completely snow free in all ensemble members were excluded from the analysis. To investigate the local and instantaneous effects, and to obtain a high confidence that the effects can actually be attributed to the aerosol deposition on snow, we performed a significance analysis.

The significance analysis focused on the significance of individual cells in the context of all paired simulations. We applied the Wilcoxon signed-rank test (Wilcoxon, 1945), testing each cell of the 40 ensemble members including the aerosol-snow-albedo interaction (SDS) against the 40 members without the interaction (REF). The test evaluates whether the two samples originate from the same distribution and returns a p-value which describes the probability of obtaining these results if the two sets originate from the same distribution. In most studies, all values where $p < 0.05$ are declared as significant results and $p < 0.01$ as highly significant results. This "naive-stippling" approach leads to many false detections of seemingly significant cells (Wilks, 2016). To minimize the false discovery rate (FDR), we applied the approach of Wilks (2016). In contrast to the stippling method, where the condition for significance is fixed to a constant p-value, this method uses a variable threshold dependent on sample size. The control level α_{FDR} was 0.2 in this study.

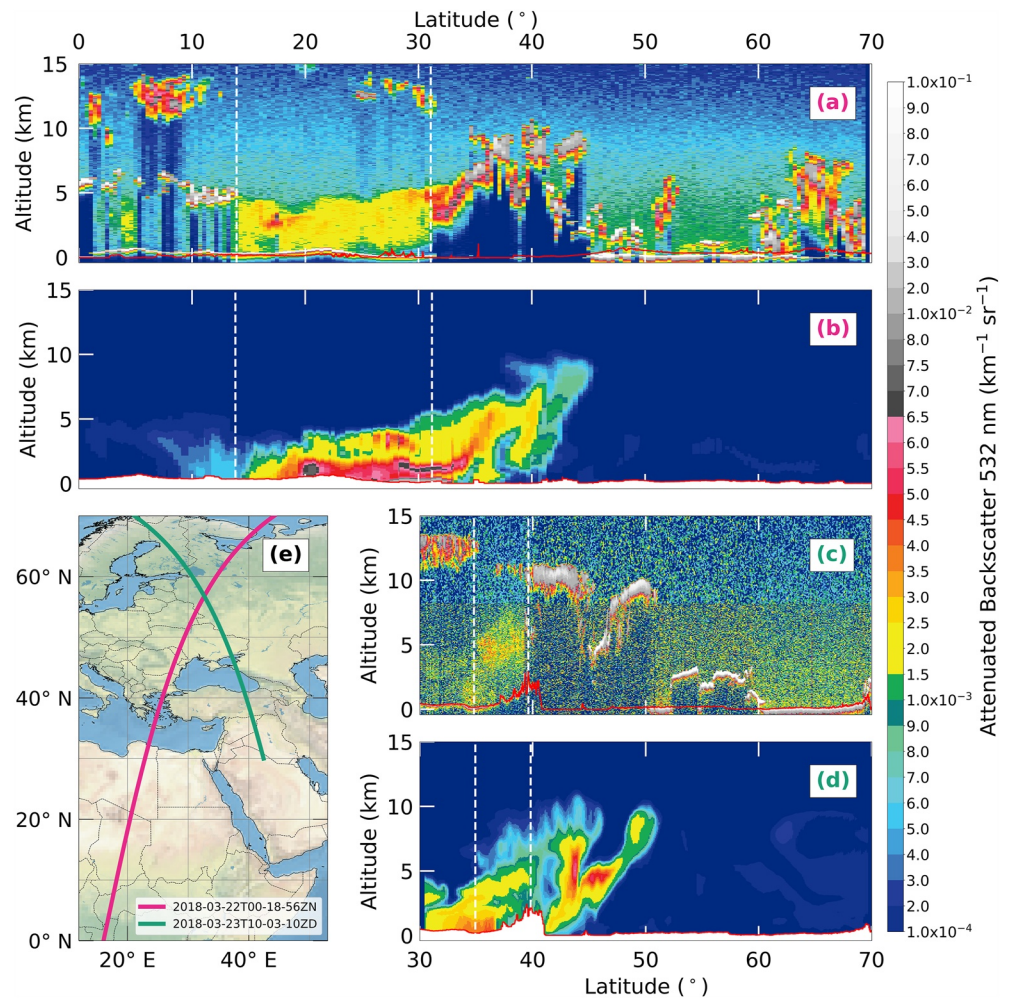### 2.4. Total Attenuated Backscatter From CALIOP

In order to verify the predicted transport of mineral dust, we compared the attenuated backscatter of the simulated mineral dust with measurements from the Cloud-Aerosol Lidar with Orthogonal Polarization (CALIOP) instrument. The instrument is a two-wavelength polarization-sensitive lidar with three receiver channels. CALIOP measures in one channel the 1,064 nm backscatter intensity and in two channels the orthogonally polarized components of the 532 nm backscatter signal. It was designed to obtain high-resolution vertical profiles of aerosols and clouds (Winker et al., 2004, 2007). The CALIOP lidar is on board the Cloud-Aerosol Lidar and Infrared Pathfinder Satellite Observations (CALIPSO) satellite. We use CALIOP Level 1 version 4.1 total attenuated backscatter at 532 nm of two measurements for validation. The first measurement was conducted on 22 March 2018, with the satellite overflying both dust source area and study region. The second observational data we considered were acquired on 23 March 2018 and include a cross section of the study area. ICON-ART comes with a forward operator for attenuated backscatter at 355, 532, and 1,064 nm that enables direct comparison of the model results with CALIOP measurements (Hoshyaripour et al., 2019). We fitted the data to the corresponding resolution of the simulation by horizontal averaging. This means that, on the one hand, we brought the initial measurement data to a horizontal resolution of about 40 km. We compared these data with the results of the global simulation, which includes the dust source area. We brought the second set of measurement data to a horizontal resolution of about 10 km. These data, on the other hand, were compared with the results of the LAM simulation.

3. Results and Discussion

In this section, we present the results in four parts. First, we show a brief comparison of the atmospheric mineral dust between simulation and remote sensing data. Then, we present the temporal evolution of the mineral dust event in the study areas A and B. This is followed by the analysis of the horizontal distribution at the time of the strongest impact of mineral dust. In the last section, we discuss the feedbacks and the regional dependencies in detail.

3.1. Validation With CALIOP Measurements

During the transport of the mineral dust in the March 2018 event, the mineral dust was well visible in various satellite images. However, the dust was largely accompanied by thick clouds. These clouds constitute a limitation for many satellite algorithms. In this case, the aerosol optical thickness observations were not suitable for model validation. Instead, we considered measurements of the total attenuated backscatter observed by the CALIOP instrument. Cloud-free regions are included in these data, from which we can draw information about the location as well as the vertical structure of the mineral dust plume. We validated our results with two individual measurements. Figure 3 shows a comparison of total attenuated backscatter measurements at 532 nm from the CALIOP instrument and the corresponding simulated attenuated backscatter of mineral dust at two different states.

Figure 3. (a) The CALIOP total attenuated backscatter for 532 nm between 0° and 70° latitude on 22 March 2018 at around 00:18 UTC, (b) the corresponding dust attenuated backscatter for 532 nm of the ICOsahedral Nonhydrostatic atmosphere and climate with Aerosols and Reactive Trace gases (ICON-ART) global simulation at 01:00 UTC, (c) the CALIOP total attenuated backscatter for 532 nm between 30° and 70° latitude on 23 March 2018 at around 10:03 UTC, (d) the corresponding dust attenuated backscatter for 532 nm of the ICON-ART Limited Area Mode model result at 10:00 UTC, and (e) the CALIPSO ground track on 22 March 2018 at 00:18 UTC in pink and on 23 March 2018 10:03 UTC in green.

Figure 3a shows the measurement on 22 March, 00:18 UTC. These observational data include the backscatter of all constituents in the atmosphere, including clouds. Thick clouds are characterized by particularly high attenuated backscatter. This extends to the point where the signal is attenuated in such manner that a measurement as far as the earth's surface is no longer possible. Such situations with strongly attenuated backscatter in great altitude appear in Figure 3a. They are visible as red to gray patches with dark blue shadows. The region between 14° and 31° latitude, indicated by the white dashed lines, remains largely free of such limitations. The respective simulation result is shown below in Figure 3b. It shows the mineral dust attenuated backscatter at 532 nm of the global ICON-ART simulation 1 hr after initialization (22 March 01:00 UTC). Solely the attenuated backscatter of mineral dust is shown here and not that of other components, such as clouds. Therefore, we initially focus on the area between 14° and 31° latitude. The horizontal as well as vertical structures of the attenuated backscatter between both figures are comparable. This region includes the northeastern part of the Sahara and thus the source area of the mineral dust. Although the structures between simulation and measurement are comparable, there is a slight difference in the intensity of the attenuated backscatter. The simulation results show a higher backscatter at ground level and a weakening of the signal up to about 4 km height. The CALIOP measurements indicate a rather constant backscatter intensity up to an altitude of 5 km. There may be several reasons for this discrepancy. For example, there could be variations in the size distribution of the mineral dust particles at emission. In this case,

this could result in different vertical distributions due to different lifting and sinking processes. Figure 3b shows that the dust plume continues north of 31° latitude toward Europe reaching an altitude of 10 km in our simulation. Unfortunately, this cannot be directly traced in the observational data due to the limitations discussed above. However, it is remarkable that the supposedly observed cloud top north of 31° has a similar structure as the top of the simulated dust plume. Since the horizontal and vertical extent of the mineral dust plume in the cloud-free region (white dashed lines) agree well, it can be assumed that this is also the case north of 31°. Furthermore, ICON-ART showed good agreements in dust transport in previous studies (Gasch et al., 2017; Hoshyaripour et al., 2019). Thus, we assume that the mineral dust is embedded under and in the clouds.

The two figures below (c and d) show the attenuated backscatter at a later time along another CALIPSO flight track. Figure 3c shows the CALIOP measurements on 23 March at 10:03 UTC. This observation is also characterized by large areas with strongly attenuated backscatter at high altitudes, most likely due to clouds. An area at approximately 35° and 40° latitude is marked (white dashed lines), where such high attenuated backscatter does not occur. Here, the increased backscatter is most likely caused by the Saharan dust particles. Increased attenuated backscatter is detected at about 3–8 km altitude. Furthermore, there is increased attenuated backscatter preceding the mountains at 35° latitude, reaching even to the ground level. Figure 3d shows the results of the LAM-simulation on 23 March at 10:00 UTC. In the region between 35° and 40° latitude the simulated attenuated backscatter of mineral dust shows a similar pattern as the total attenuated backscatter observed by the CALIOP instrument. The dust plume extends to an altitude of about 8 km and is visible at ground level at about 35° latitude. Near the ground, the simulated attenuated backscatter is slightly stronger compared to the observation. Due to the proximity to further sources, deviations in the emission parameters, such as size distribution, might have an influence on the deviation of backscatter intensity. The simulation results show, north of 40° latitude, the dust plume propagates and reaches 50° latitude. Unfortunately, again we cannot draw a direct comparison in the observational data due to constraints. However, it is again clearly visible that the upper boundary of the signal in the CALIOP data, which is presumably caused by clouds, corresponds to the pattern of the upper boundary of the simulated dust plume. We conclude that the mineral dust is located inside and below the clouds. Due to the similar patterns and the agreement between 35° and 40° latitude the simulation results appear plausible. At approximately 41° latitude, the simulated dust plume reaches the ground level. In this region, close to the Caucasus Mountains, we can identify the dust deposition in the simulation results (Figure 3b). Figure 3e shows the two overflight paths of CALIPSO and the lidar measurements corresponding to figures (a) and (b) in pink and (c) and (d) in green.

3.2. Temporal Evolution in Region A and B

The course of the Saharan dust event was summarized by Barkan and Alpert (2020). A cold through extended from Scandinavia to Western Sahara. This caused a severe dust storm that lifted huge amounts of Saharan dust in the air. Southwesterly flows transported the mineral dust particles within 2 days to Eastern Europe. In the morning of 23 March 2018, the dust deposited together with snow. The chemical composition of samples taken on March 24 near Bucharest, Romania, indicated the Northern Sahara as the dust source (Marmureanu et al., 2019). Figure 4 shows (a) the simulated temporal evolution of mineral dust mass in the top snow layer, (b) the differences between SDS and REF in diffuse surface albedo, (c) surface shortwave net radiation flux, (d) snow depth, (e) surface temperature, and (f) 2 m temperature. These are results of the study region A extending over the Caucasus Mountains (red) and region B focusing on the extended area containing the snow line (blue). Depicted are the spatially averaged hourly results.

Wet deposition of mineral dust was observed in the Caucasus region (Sochi) in the morning of 23 March 2018. The transport of Saharan dust ceased from March 24 to March 25 but strengthened again from March 26 to March 27 (Barkan & Alpert, 2020). Our results indicate an increase in the mean mineral dust mass in the top snow layer from March 23 onward. The mean dust loading in region A reaches the first maximum of 0.6 g m^{-2} on March 24, 13 UTC. After that, dust-free precipitation reduced the average dust loading in the top snow layer. As reported by Barkan and Alpert (2020), further Saharan dust transport occurred from March 26. The simulated daily mean dust loading over the whole region A reaches a maximum on March 29 at 9 UTC (0.9 g m^{-2}). Thereafter, the mean dust concentration drops rapidly as the dust was covered anew by dust-free snowfall.

The difference between SDS and REF in surface albedo develops with the accumulation of mineral dust in region A. A first maximum in the reduction in surface albedo is reached on March 24, 14 UTC. The reduction in surface
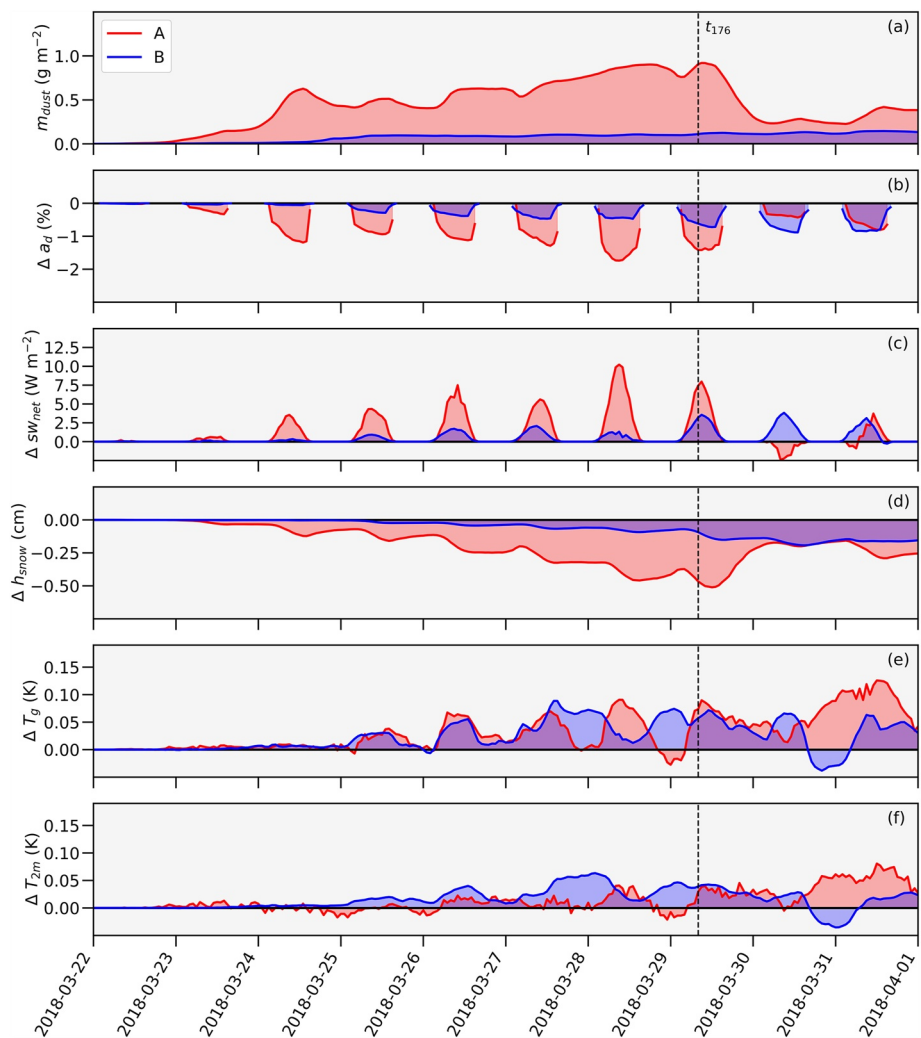
Figure 4. (a) Spatially averaged hourly simulation results of mineral dust deposition in the top snow layer, (b) the differences (snow-darkening simulation−reference experiment) in surface albedo, (c) surface shortwave net radiation flux, (d) snow depth, (e) surface temperature, and (f) 2 m temperature across region A (red) and B (blue).

albedo due to mineral dust is at that point −1.2%. In the later stages, the surface albedo experiences even greater reductions. On March 28, 9 UTC and March 29, 9 UTC further maxima are reached with a decrease ranging up to −1.7% and −1.4%, respectively. The overall mean reduction in surface albedo during sunlit hours in region A is −0.7%. The largest daily reduction in surface albedo occurs on March 28, with an average difference of −1.4%.

The increase in surface shortwave net radiation flux grows from day-to-day with the decrease in surface albedo. The influence is strongest at the peak of sun elevation. However, the occurrence of the phenomenon depends on the prevailing conditions. For example, the radiative effect at the surface can be negative despite the reduced surface albedo. This happens when the cloud cover or the precipitation differs in the two experiments. This is the case after March 29. The shortwave net radiation flux shows that both experiments diverge in the atmospheric conditions. Therefore, we focus on March 29 for the more detailed spatial analysis. On March 29, the daily maximum in region A reaches a difference of 8.0 W m^{-2}. However, the overall maximum is already reached on March 28 with a difference of 10.2 W m^{-2}.

Figure 4d shows that the difference in snow depth between the two experiments increases during daytime. Throughout the dust event, the difference in region A continues to grow until March 29. At this point, the maximum difference of −0.5 cm is reached. Due to fresh snowfall without mineral dust, the difference decreases again after this day.
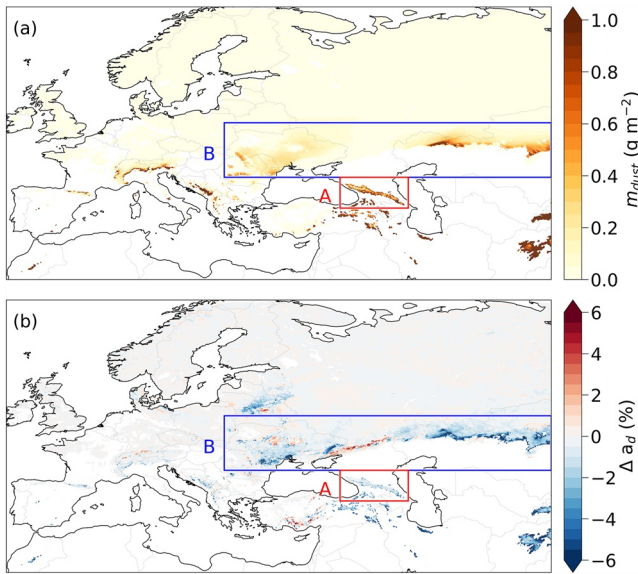
Figure 5. (a) Distribution of the ensemble mean dust loading in the top snow layer in snow-darkening simulation (SDS) and (b) the ensemble mean difference in diffuse surface albedo between SDS and reference experiment on 29 March 2018, 8 UTC.

The differences between SDS and REF in surface temperature and 2 m temperature indicate that the relationship with mineral dust deposition is somewhat more complicated than the relationship between surface albedo or surface shortwave net radiation flux with dust accumulation. There are many fluctuations, but mainly warming occurs in the SDS experiment. Similar to the previous variables, the largest differences occur around midday. The strongest increase in the two variables is reached on the last 2 days. Here, however, it is uncertain whether this warming was induced directly by the mineral dust deposition. Opposed to this is the fact that the difference in shortwave radiation absorption is only moderate. If we exclude the last 2 days, the largest temperature increase occurs on March 29. Here, the increase in surface temperature and 2 m temperature reaches an extent of 0.09 and 0.05 K, respectively. That means, on average the temperature changes in the lowest layer of the atmosphere are quite small.

Region B was less affected by the Saharan dust event and shows less variability in the temporal analysis. The accumulation of mineral dust in the top snow layer gradually increases and reaches a maximum value of 0.15 g m^{-2} on the last simulation day. The mean difference in surface albedo between the two experiments increases with each passing day. The albedo reduction due to Saharan dust averaged over the course of the day is largest on March 30 and reaches −0.9% in region B. The largest radiative forcing occurs on the last three simulation days. At the daily maximum an additional surface shortwave net radiation flux of 3.3, 3.8, and 3.1 W m^{-2} occurs on March 29, 30, and 31, respectively. The strongest decrease in snow depth occurred in region B on March 30, with a difference of −0.2 cm. High variability in the differences in surface temperature and 2 m temperature is also evident in this region. The difference in surface temperature ranges between −0.04 and 0.09 K over the entire period. However, there is a warming of the surface for 89% of the simulated time span. The difference in 2 m temperature varies between −0.04 and 0.06 K. We found no significant effect on cloud cover or precipitation in the temporal analysis in either region A or B (not shown).

It is apparent that the formation of feedback in the different variables requires a certain leading time. The largest differences between SDS and REF appear in region B on the last day, indicating that the repercussions have not reached a threshold within the simulated 10 days and possibly may even expand. This depends on the development of the weather conditions. An important aspect to consider here is that the snow in our simulation is completely aerosol free at the initial stage. This could lead to an underestimation of the dust loading in snow since background concentrations that accumulated before the major dust event are not captured. Dumont et al. (2020) reported that the dust deposition was covered by clean snow after a few days in the Caucasus. We found the same in our simulation results. With large amounts of new snow, the effect of mineral dust on snow can be quickly removed. However, Dumont et al. (2020) stated that with snow melting after a few weeks, the aerosols were again exposed and concentrated at the snow surface. As a result, the deposited mineral dust again had an impact on snow melt. This means that the effects of an extreme dust deposition event are not only of short duration but can have far-reaching consequences for the snow cover during the whole season. We found the strongest feedbacks in almost all variables around midday. An exception is the snow depth. Here the greatest reduction is shifted to the end of the day.

3.3. Spatial Distribution

Figure 5 shows the ensemble mean distribution of mineral dust in the top snow layer in SDS (a) and the ensemble mean difference in diffuse surface albedo between SDS and REF on snow-covered surfaces (b) on March 29, 8 UTC, after 176 hr of simulation (t_{176}). Mineral dust mainly accumulates on mountain ranges. This is clearly visible on the south-facing slopes of the Pyrenees, the Alps, the Dinaric Mountains, and the Carpathians. In addition, the Caucasus Mountains and parts of the Pontic Mountains adjacent to them in the south have high levels of mineral dust in snow. In the southeast of the model domain, parts of the Hindu Kush and the Pamirs are identifiable. They show a higher influence by mineral dust, but are not in the focus of this study. Surprisingly, higher levels of
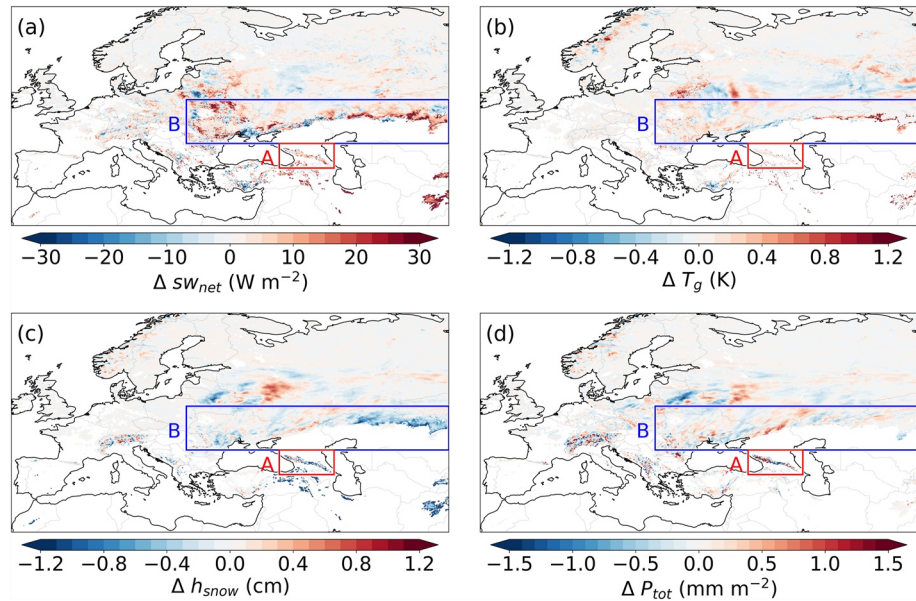
Figure 6. Distribution of the ensemble mean differences in surface shortwave net radiation flux (a), surface temperature (b), snow depth (c), and total precipitation (d), between snow-darkening simulation and reference experiment on 29 March 2018, 8 UTC.

mineral dust are present along the snow line in Kazakhstan, although the terrain is rather flat. This is connected to higher surface concentration due to the successive melting back of the snow line. The mean dust loading of the whole model domain at t_{176} is 0.1 g m^{-2} with a local maximum of 32.9 g m^{-2} (Baba Mountain range, western extension of the Hindu Kush). Region A has a mean dust loading of 0.9 g m^{-2} and a local maximum of 11.7 g m^{-2} at this point. Region B has a mean dust loading of 0.1 g m^{-2} and a local maximum of 1.7 g m^{-2}.

The patterns of ensemble mean difference in diffuse snow albedo between SDS and REF show similarities to the mineral dust distribution (Figure 5b). The largest differences in surface albedo between the two experiments are mainly apparent at places with higher dust concentrations. Thus, complex terrain is strongly affected by a reduction in surface albedo. The areas along the snow line also show a strong reduction except for an area in Russia northeast of the Black Sea. The area of the Caucasus Mountains shows a particularly clear negative signal in diffuse surface albedo as well. Furthermore, areas in the northwestern corner of the Black Sea as well as some areas in Belarus are characterized by reduced surface albedo in SDS. The ensemble mean reduction in surface albedo in SDS is −0.4% over the whole area, −1.4% in region A and −0.6% in region B. The respective standard deviations are 1.2%, 1.5% in region A and 1.5% in region B. The values of the strongest reduction in these areas are correspondingly −38.4%, −13.4%, and −16.0%.

Figure 6 shows the ensemble mean difference patterns of surface shortwave net radiation flux (a), surface temperature (b), snow depth (c), and total precipitation (d) between SDS and REF on snow-covered surfaces on March 29, 8 UTC, after 176 hr of simulation (t_{176}). The signal in surface shortwave net radiation flux appears relatively chaotic. There are several areas where an increase in the radiation flux appears, but there are also areas where the radiation flux decreases. This is mainly due to the pattern of the cloud cover. A slight shift of the location of the clouds already results in strong signals. Particularly in Eastern Europe, a noisy pattern is evident that is not related to mineral dust deposition or changes in surface albedo. The surfaces in the Caucasus Mountains as well as in areas near the snow line are characterized by a strong increase in shortwave radiation flux. An exception is an area northeast of the Black Sea, where a decline occurs. There is a clear positive radiative forcing when considering spatial averages. At t_{176}, the difference between SDS and REF is 1.5 W m^{-2} in the whole study region, 7.4 W m^{-2} in region A and 3.2 W m^{-2} in region B.

The difference in surface temperature between the two experiments is illustrated in Figure 6b. A strong increase in surface temperature due to mineral dust deposition is almost exclusively evident along the snow line. Northeast of the Black Sea, the surface temperature in SDS is in turn lower. The increased surface albedo also occurs at this

location (Figure 5b). But there are differences, especially on the Russian territory, that cannot be attributed to the changes in albedo and do not exactly match the patterns of the other variables that have been shown. A temporal analysis of the spatial distribution showed that these patterns are constantly shifting. During the simulation, such patterns are headed toward various directions and are most pronounced during the day. There is no explicit tendency to a decrease or increase here. We assume that these patterns are caused by atmospheric dynamics rather than surface properties. Nevertheless, on average, a slightly higher surface temperature is apparent in SDS. The mean difference in surface temperature over the whole area is 0.03 K. The regional surface temperature difference between SDS and REF is 0.07 K in A and 0.06 K in B. In the latter region, the warming reaches locally up to 2.72 K. The feedback in 2 m temperature has very similar patterns compared to the surface temperature (not shown). However, the amplitude mostly reaches only half as large values as the feedback of the surface temperature. The spatially averaged 2 m temperature difference in the whole study region is 0.01 K, 0.03 K in region A, and 0.04 K in region B, which is quite small.

The variation in snow depth is among other factors strongly influenced by precipitation patterns. Differences in snow depth and total precipitation are shown in Figures 6c and 6d, respectively. In particular, the patterns of both variables on Russian territory, Belarus, and Ukraine match up very accurately. This allows the assumption that random changes in precipitation patterns cause these deviations in snow depth. Alternately, both an increase and a decrease in snow depth occur, with the decrease predominating in Belarus. This decrease explains the reduction in surface albedo at this location. A thinning of the snow pack reduces the surface albedo, since the ground underneath contributes to a larger extent to the overall albedo. The reduction in surface albedo here relates only to a negligible extent to the deposition of mineral dust. However, there are widespread areas where a modification in snow depth cannot be accounted for by the changes in precipitation. They can be attributed to the perturbation of the optical properties of snow due to mineral dust. They coincide with the decrease in surface albedo in SDS. For instance, a reduction in snow depth is mainly observed in the Caucasus Mountains and the mountains further south and east. Furthermore, a decrease in snow depth near the snow line is mainly apparent. Again, an exception is an area in Russia northeast of the Black Sea. Here, an increase in precipitation explains the increase in snow depth and surface albedo. The mean difference in snow depth over the whole study region at t_{176} is −0.1 cm. The strongest local feedback of snow depth is in the French Alps, resulting in a reduction of −10.2 cm. Hence, although the temperature changes appear small, the snow depth decreases substantially.

The distributions in Figures 5 and 6 show that there are direct feedbacks on several variables due to mineral dust deposition. Therefore, a relatively clear and consistent pattern appears. The difference in snow depth shows a cumulative effect of mineral dust on snow cover. Therefore, a relatively clear and consistent pattern appears. In contrast, the differences in net shortwave radiation flux, surface temperature, and 2 m temperature show an instantaneous effect. Various other influences, such as atmospheric dynamics, can interfere with these instantaneous mineral dust effects. To assess the significance of our results, we applied the Wilcoxon signed-rank test (Wilcoxon, 1945) and the false discovery rate control of Wilks (2016) on the surface albedo differences. Figure 7 shows the significant surface albedo differences between SDS and REF at t_{176}. We found that only the reduction in surface albedo is statistically significant and caused by mineral dust deposition. These significant reductions are mainly limited to the regions A and B and some mountain ranges in Eurasia. The strongest signals occur mainly where the snow cover is particularly thin, for example, in Kazakhstan. The mean significant reduction in surface albedo at t_{176} is −2.2% over the whole study area, and −1.9% and −2.3% in regions A and B, respectively. Increases in surface albedo in our simulation results are not statistically significant.

3.4. Local Implications on the Atmosphere and Land Surface

In this section, we examine statistical relationships between snow-darkening and the differences in atmospheric and land surface variables. Here, our analysis is based on statistically significant results only. Figure 8 shows the statistical relationships between (a) mineral dust deposition and the impact on surface albedo. Furthermore, it shows the (b) relationship between the impact on surface albedo and the impact on the variables surface shortwave net radiation flux, (c) snow depth, and (d) surface temperature. The four density scatter plots illustrate the frequency of the occurrences at t_{176} throughout the whole simulation domain. In addition, the linear regression line is indicated as dashed red line.

Figure 8a shows that the reduction in surface albedo cannot be explained directly from mineral dust deposition only. The Pearson R correlation coefficient is −0.67 and the results scatter throughout the lower half of the figure.
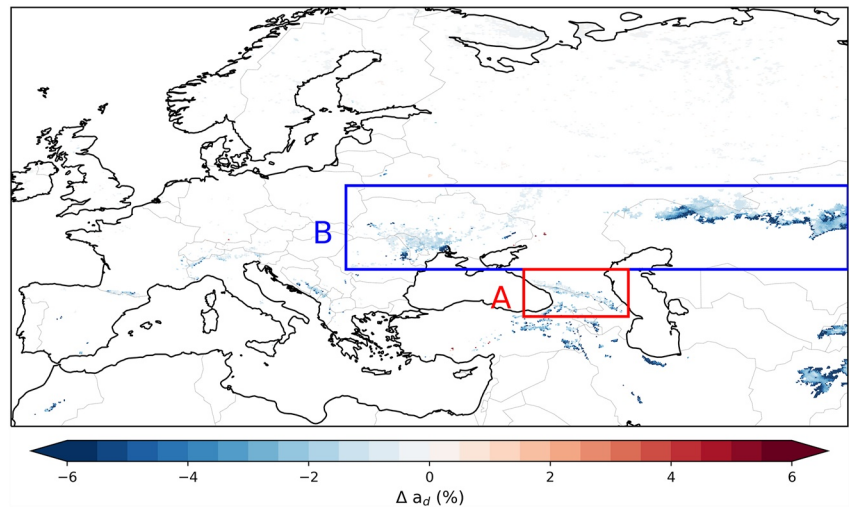
Figure 7. Spatial distribution of statistically significant ensemble mean differences between snow-darkening simulation and reference experiment in diffuse surface albedo on 29 March 2018, 8 UTC.

For example, there are many locations where the mineral dust deposition is below 1 g m^{-2}, but the reduction in surface albedo reaches an extend of -15%. On the other hand, there are locations where the mineral dust deposition is above 3 g m^{-2}, but the albedo is affected by less than -1%. This seems contradictory at first glance, but it has already been found in previous studies that not only aerosol deposition but also the condition of the snow
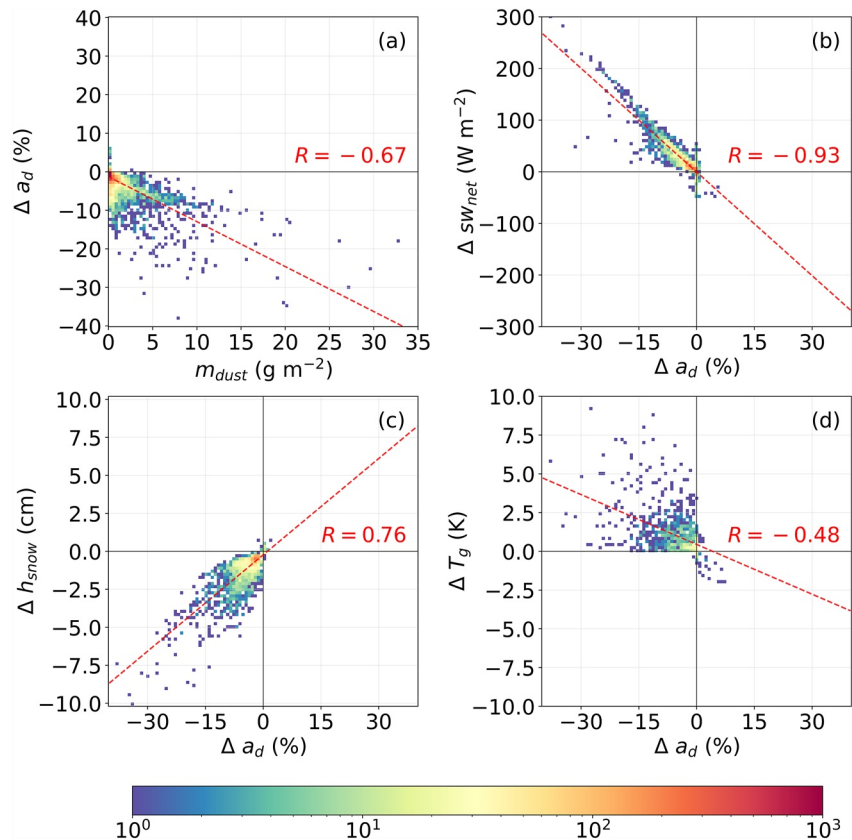
Figure 8. (a) Density scatter plots of significant local ensemble mean differences in diffuse surface albedo between snow-darkening simulation (SDS) and reference experiment (REF) in relation to dust loading in the top snow layer in SDS, (b) the significant local differences in surface shortwave net radiation flux, (c) snow depth, (d) surface temperature, in relation to differences in diffuse surface albedo between SDS and REF on 29 March 2018, 8 UTC.

plays an important role. For example, the overall reduction in snow albedo is greater if the snow is aged or if there are multiple layers of dust overlapping (Lamare et al., 2016; Skiles et al., 2018; Warren & Wiscombe, 1980). An additional reason could be the sinking of aerosols into the snow layer. Our approach is to have a uniform distribution of the dust concentration within the first 10 cm. This leads to a lower concentration of deep snow compared to a thin layer of snow. Although this sinking is not parameterized in more detail in our model, such sinking of aerosols has been observed during measurements in previous studies (Peltoniemi et al., 2015; Svensson et al., 2016). A clear linear relationship exists between the feedback in surface shortwave net radiation flux and reduction in surface albedo (Figure 8b). Here, the correlation coefficient is −0.93. Hence, a reduction in surface albedo is associated with a clear enhancement of solar energy absorption. Biases in the results can arise in this comparison if the cloud cover differs between SDS and REF. We further found a linear relationship between melting of snow and reduction in surface albedo (Figure 8c). The comparison results in a correlation coefficient of 0.76. Since the coefficient is not close to unity, it suggests that other factors also have an influence on melting. Since we found the strongest feedback in areas near the snow line, where snow cover is patchy and thin, we assume a dependence of the variables on the prevailing snow depth. We discuss this further below. We found the weakest correlation between the feedback of surface temperature (Figure 8d) and 2 m temperature (latter not shown) to surface albedo. The correlation coefficients are −0.48 and −0.54, respectively. As previously indicated in the spatial analysis, the two variables have weak feedbacks to snow-darkening, which in turn are easily superimposed by other signals.

Figure 9 represents a similar illustration as Figure 8. In this case, however, (a) the feedbacks of surface albedo, (b) surface shortwave net radiation flux, (c) snow depth, and (d) surface temperature are compared to the prevailing snow depth. We cannot derive any linear relationship here. However, we can identify a dependence of the feedbacks. The intensity is particularly strong at shallow snow depths. This is most noticeable when considering the reduction in surface albedo and the increase in surface temperature. The former shows strong signals with shallow and deep snow cover. However, it appears that the reduction is most pronounced at a snow cover of a few centimeters. We believe that the snow-albedo feedback plays a larger role here. The amplification of the feedback is due to the uncovering of the darker ground below the snow. The same process probably causes a slight increase in the absorption of shortwave radiation at shallow snow depths. Furthermore, the surface temperature shows feedbacks almost exclusively at low snow depths of a few centimeters. It is important to consider that the analyzed snow depth is an ensemble mean. This means that it is possible that in individual runs the thin snow cover has already melted due to the mineral dust. The exposed land surface can then heat up more (several degrees) in contrast to the snow-covered surfaces. This explains the large dependence of surface temperature changes on snow depth. The effect on snow melting, in contrast, shows a smaller dependence on the current snow depth. Melting is intensified when the snow cover is thin, but strong feedbacks can also occur with deep snow cover of 1 m.

We demonstrate the dependence on the state of snow cover by means of the quantification of the feedbacks in the regions A and B. Table 1 displays the spatial averages of the significant differences between SDS and REF in surface shortwave net radiation flux, snow depth, surface temperature, and 2 m temperature. The spatial mean of the corresponding surface albedo differences are presented alongside.

Region A includes the Caucasus Mountains. Thus, the terrain is complex. The snow cover is rather thick and closed. The impact on the absorption of shortwave radiation is stronger in region A. There is an increase in surface shortwave net radiation flux by 18.47 W m^{-2}. This additional energy is mainly reflected in snow melt. The snow depth is reduced here by −1.36 cm on average. The surface temperature and the 2 m temperature, however, show a weaker signal in region A. It should be noted that complex terrain holds larger uncertainties compared to flat terrain, for example, shading effects due to topography are present (Hao et al., 2021; Olson & Rupper, 2019) that were not considered in this study. In region B, which is mainly characterized by flat areas in Kazakhstan, the reduction in snow depth is lower with a mean decrease of −0.60 cm. The increase in surface shortwave net radiation flux amounts 15.96 W m^{-2}. However, there is a stronger warming of the land surface and the near-surface atmosphere in region B. The increase in surface temperature and 2 m temperature is on average 0.92 and 0.49 K, respectively.

4. Conclusions

We improved the model ICON-ART by implementing a new snow albedo parametrization following Wiscombe and Warren (1980) and Warren and Wiscombe (1980). The new developments enable the computation of a
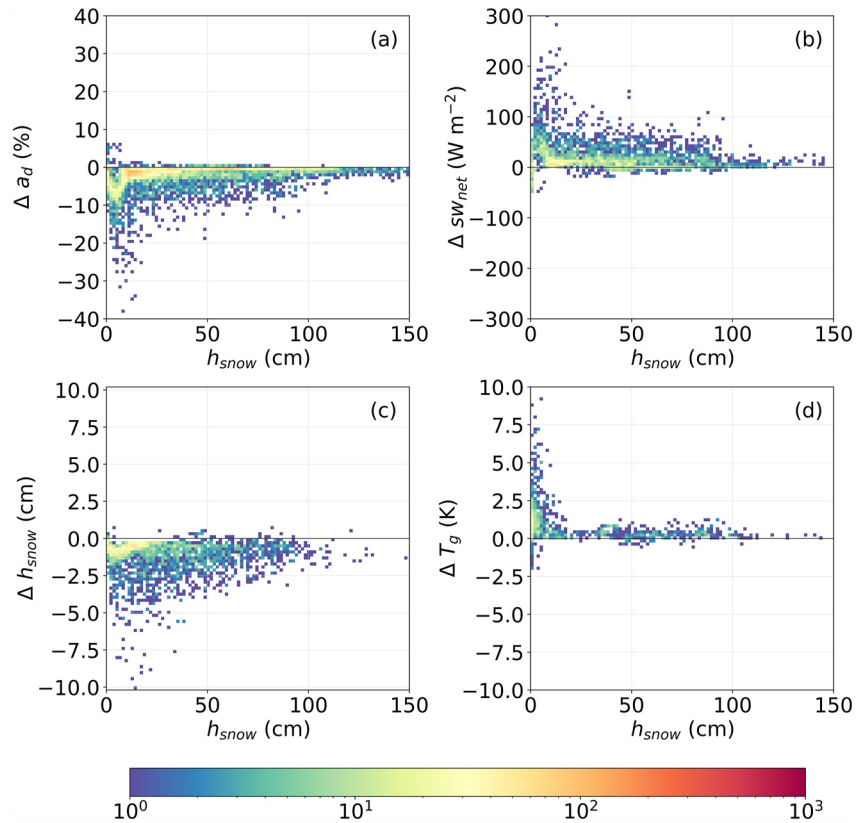
Figure 9. (a) Density scatter plots of significant local differences between snow-darkening simulation and reference experiment in diffuse surface albedo, (b) surface shortwave net radiation flux, (c) snow depth, and (d) surface temperature, in relation to the apparent snow depth on 29 March 2018, 8 UTC.

spectral snow albedo in 18 shortwave bands. We included mineral dust optical properties of ICON-ART in our developments to investigate its impact on the snow albedo. In our simulations, the deposition of mineral dust affects the optical properties of the snow surface online. Postdepositional processes such as sinking of mineral dust particles into the snowpack and resurfacing are accounted for.

We conducted a case study to analyze the impact of mineral dust deposition on the spectral snow albedo during a large Saharan dust deposition event. This event occurred in spring 2018 and affected snow surfaces in Eastern Europe and western parts of Asia. Emission, transport, deposition, and impact of mineral dust were computed online in the experiment. We applied an ensemble simulation with a total of 80 ensemble members to investigate the impact during this intensive event. Furthermore, we obtained evidence of statistical significance by applying the Wilcoxon signed-rank test (Wilcoxon, 1945) and the significance evaluation described by Wilks (2016).

We analyzed the spatial distribution of mineral dust and associated feedbacks during this event in Eurasia to answer the question, whether the distribution of mineral dust results in the formation of particularly vulnerable regions. We found that dust loading in snow is spatially highly variable and affects certain regions with particular severity. Mountainous regions and a relatively flat area in Kazakhstan were primarily affected. The former showed particularly severe contamination with dust particles, especially on the southwestern slopes. The latter is probably strongly influenced due to the proximity to dust sources and melting processes at the snow line. Here the snow-albedo feedback plays a larger role. Through the particularly thin snow layer in this

Table 1

Spatial Average of the Statistically Significant Feedback in Surface Shortwave Net Radiation Flux sw_{net}, Snow Depth h_{snow}, Surface Temperature T_g, and 2 m Temperature T_{2m} in Regions A and B and Associated Changes in Diffuse Surface Albedo After 176 hr of Simulation on 29 March 2018, 8 UTC

Var	Region	Mean of significant differences	Mean of associated surface albedo differences
Δsw_{net}	A	18.47 W m^{-2}	−2.72%
	B	15.96 W m^{-2}	−2.50%
Δh_{snow}	A	−1.36 cm	−2.83%
	B	−0.60 cm	−3.41%
ΔT_g	A	0.69 K	−3.96%
	B	0.92 K	−4.50%
ΔT_{2m}	A	0.30 K	−4.57%
	B	0.49 K	−4.20%

region, the darker ground below the snow gets more influence in the total albedo. It is therefore highly important to simulate aerosol emission, transport and deposition online to achieve a proper distribution of the mineral dust. The temporal evolution of the snow cover plays an important role as it determines whether the aerosols sink in with new snowfall or concentrate on the snow surface due to snow melt. Our results show that larger amounts of clean fresh snow can rapidly offset the effects of mineral dust.

The second question we set out to answer is as follows: How intense can the feedbacks in the land surface and the atmosphere be during a severe dust event? We found that the mineral dust causes a statistically significant reduction in surface albedo and snow depth as well as a statistically significant increase in surface shortwave net radiation flux, surface temperature, and 2 m temperature. In individual locations, strong feedbacks can occur. In the case of the surface albedo, for example, the reduction extended to -38.4% and the reduction in snow depth to -10.2 cm. However, these are extreme cases. On average, the reduction in surface albedo was -2.7% and the reduction in snow depth was -1.36 cm in the Caucasus region. The increase in shortwave net radiation flux in the region averaged 18.47 W m^{-2}.

The final question we address in this study is which surface and atmospheric variables are most strongly affected during this event. We found a strong regional dependence of the feedbacks, mainly due to the state of the snow cover. In a thick, closed snow pack, additional absorbed shortwave radiation leads to snow melt. We found this relationship mainly in mountainous areas. With thin snow cover, the radiative forcing leads to warming of the surface and air temperature instead. The reason for this is that dust deposition coincides with patchy and thin snow. Snow melt also occurs in these areas, but the solar energy is more likely to melt away the snow cover and reach the land surface. The energy that reaches the ground causes strong warming of the surface. However, this feedback remains rather small compared to the effects on surface albedo, shortwave net radiation flux, and snow depth. In the region along the snow line, the mean increase in surface temperature was 0.9 K and the increase in 2 m temperature was 0.49 K.

In conclusion, to estimate the responses to the snow-darkening effect, it is important to consider the aspects of exposure to dust deposition, altitude, and snow coverage of the study region. Mountain ranges are especially affected by mineral dust deposition, in particular the south facing slopes in this case. The resulting response is mainly the reduction in snow cover. Moreover, the snow line in Eurasia is one of the most sensitive regions despite the flat area since the snow cover fraction is small. This leads mainly to a surface warming because of the accelerated retreat of the snow line to the north and exposure of the darker ground.

Conflict of Interest

The authors declare no conflicts of interest relevant to this study.

Data Availability Statement

The ensemble mean values from the ICON-ART simulations performed for this study and the results of the statistical analysis are available at RADAR4KIT via https://doi.org/10.35097/1579 with "CC B-YND 4.0" (Rohde, 2023). The used ICON-ART code is license protected and can be accessed by request to the corresponding author.

References

Aoki, T., Motoyoshi, H., Kodama, Y., Yasunari, T. J., Sugiura, K., & Kobayashi, H. (2006). Atmospheric aerosol deposition on snow surfaces and its effect on albedo. *Scientific Online Letters on the Atmosphere*, *2*, 13–16. https://doi.org/10.2151/sola.2006-004

Barkan, J., & Alpert, P. (2020). Red snow occurrence in Eastern Europe. A case study. *Weather*, *75*(2), 45–48. https://doi.org/10.1002/wea.3644

Bartelt, P., & Lehning, M. (2002). A physical SNOWPACK model for the Swiss avalanche warning: Part I: Numerical model. *Cold Regions Science and Technology*, *35*(3), 123–145. https://doi.org/10.1016/s0165-232x(02)00074-5

Brun, E., David, P., Sudul, M., & Brunot, G. (1992). A numerical model to simulate snow-cover stratigraphy for operational avalanche forecasting. *Journal of Glaciology*, *38*(128), 13–22. https://doi.org/10.1017/s0022143000009552

Bryant, A. C., Painter, T. H., Deems, J. S., & Bender, S. M. (2013). Impact of dust radiative forcing in snow on accuracy of operational runoff prediction in the Upper Colorado River Basin. *Geophysical Research Letters*, *40*(15), 3945–3949. https://doi.org/10.1002/grl.50773

Dang, C., Fu, Q., & Warren, S. G. (2016). Effect of snow grain shape on snow albedo. *Journal of the Atmospheric Sciences*, *73*(9), 3573–3583. https://doi.org/10.1175/jas-d-15-0276.1

Deems, J. S., Painter, T. H., Barsugli, J. J., Belnap, J., & Udall, B. (2013). Combined impacts of current and future dust deposition and regional warming on Colorado River Basin snow dynamics and hydrology. *Hydrology and Earth System Sciences*, *17*(11), 4401–4413. https://doi.org/10.5194/hess-17-4401-2013

Di Mauro, B., Garzonio, R., Rossini, M., Filippa, G., Pogliotti, P., Galvagno, M., et al. (2019). Saharan dust events in the European Alps: Role in snowmelt and geochemical characterization. *The Cryosphere*, *13*(4), 1147–1165. https://doi.org/10.5194/tc-13-1147-2019

Doms, G., Förstner, J., Heise, E., Herzog, H., Mironov, D., Raschendorfer, M., et al. (2018). *A description of the nonhydrostatic regional cosmo model. Part II: Physical parameterization*. Deutscher Wetterdienst.

Donth, T., Jäkel, E., Ehrlich, A., Heinold, B., Schacht, J., Herber, A., et al. (2020). Combining atmospheric and snow radiative transfer models to assess the solar radiative effects of black carbon in the Arctic. *Atmospheric Chemistry and Physics*, *20*(13), 8139–8156. https://doi.org/10.5194/acp-20-8139-2020

Dumont, M., Brun, E., Picard, G., Michou, M., Libois, Q., Petit, J. R., et al. (2014). Contribution of light-absorbing impurities in snow to Greenland's darkening since 2009. *Nature Geoscience*, *7*(7), 509–512. https://doi.org/10.1038/ngeo2180

Dumont, M., Tuzet, F., Gascoin, S., Picard, G., Kutuzov, S., Lafaysse, M., et al. (2020). Accelerated snow melt in the Russian Caucasus mountains after the Saharan dust outbreak in march 2018. *Journal of Geophysical Research: Earth Surface*, *125*(9), e2020JF005641. https://doi.org/10.1029/2020jf005641

Essery, R., Best, M., & Cox, P. (2001). Moses 2.2 technical documentation [Report].

Flanner, M. G., Liu, X., Zhou, C., Penner, J. E., & Jiao, C. (2012). Enhanced solar energy absorption by internally-mixed black carbon in snow grains. *Atmospheric Chemistry and Physics*, *12*(10), 4699–4721. https://doi.org/10.5194/acp-12-4699-2012

Flanner, M. G., & Zender, C. S. (2005). Snowpack radiative heating: Influence on Tibetan Plateau climate. *Geophysical Research Letters*, *32*(6), L06501. https://doi.org/10.1029/2004gl022076

Flanner, M. G., Zender, C. S., Hess, P. G., Mahowald, N. M., Painter, T. H., Ramanathan, V., & Rasch, P. (2009). Springtime warming and reduced snow cover from carbonaceous particles. *Atmospheric Chemistry and Physics*, *9*(7), 2481–2497. https://doi.org/10.5194/acp-9-2481-2009

Fujita, K. (2007). Effect of dust event timing on glacier runoff: Sensitivity analysis for a Tibetan glacier. *Hydrological Processes*, *21*(21), 2892–2896. https://doi.org/10.1002/hyp.6504

Gasch, P., Rieger, D., Walter, C., Khain, P., Levi, Y., Knippertz, P., & Vogel, B. (2017). Revealing the meteorological drivers of the September 2015 severe dust event in the Eastern Mediterranean. *Atmospheric Chemistry and Physics*, *17*(22), 13573–13604. https://doi.org/10.5194/acp-17-13573-2017

Gautam, R., Hsu, N. C., Lau, W. K. M., & Yasunari, T. J. (2013). Satellite observations of desert dust-induced Himalayan snow darkening. *Geophysical Research Letters*, *40*(5), 988–993. https://doi.org/10.1002/grl.50226

Giorgetta, M. A., Brokopf, R., Crueger, T., Esch, M., Fiedler, S., Helmert, J., et al. (2018). ICON-A, the atmosphere component of the ICON Earth system model: I. Model description. *Journal of Advances in Modeling Earth Systems*, *10*(7), 1613–1637. https://doi.org/10.1029/2017ms001242

Hansen, J. (2005). Efficacy of climate forcings. *Journal of Geophysical Research*, *110*(D18), D18104. https://doi.org/10.1029/2005jd005776

Hansen, J., & Nazarenko, L. (2004). Soot climate forcing via snow and ice albedos. *Proceedings of the National Academy of Sciences of the United States of America*, *101*(2), 423–428. https://doi.org/10.1073/pnas.2237157100

Hao, D., Bisht, G., Gu, Y., Lee, W.-L., Liou, K.-N., & Leung, L. R. (2021). A parameterization of sub-grid topographic effects on solar radiation in the E3SM Land Model (version 1.0): Implementation and evaluation over the Tibetan Plateau. *Geoscientific Model Development*, *14*(10), 6273–6289. https://doi.org/10.5194/gmd-14-6273-2021

Hoshyaripour, G. A., Bachmann, V., Förstner, J., Steiner, A., Vogel, H., Wagner, F., et al. (2019). Effects of particle nonsphericity on dust optical properties in a forecast system: Implications for model-observation comparison. *Journal of Geophysical Research: Atmospheres*, *124*(13), 7164–7178. https://doi.org/10.1029/2018jd030228

Jacobi, H. W., Lim, S., Ménégoz, M., Ginot, P., Laj, P., Bonasoni, P., et al. (2015). Black carbon in snow in the upper Himalayan Khumbu Valley, Nepal: Observations and modeling of the impact on snow albedo, melting, and radiative forcing. *The Cryosphere*, *9*(4), 1685–1699. https://doi.org/10.5194/tc-9-1685-2015

Jacobson, M. Z. (2004). Climate response of fossil fuel and biofuel soot, accounting for soot's feedback to snow and sea ice albedo and emissivity. *Journal of Geophysical Research*, *109*(D21), D21201. https://doi.org/10.1029/2004jd004945

Jäkel, E., Carlsen, T., Ehrlich, A., Wendisch, M., Schäfer, M., Rosenburg, S., et al. (2021). Measurements and modeling of optical-equivalent snow grain sizes under arctic low-sun conditions. *Remote Sensing*, *13*(23), 4904. https://doi.org/10.3390/rs13234904

Kaspari, S., Painter, T. H., Gysel, M., Skiles, S. M., & Schwikowski, M. (2014). Seasonal and elevational variations of black carbon and dust in snow and ice in the Solu-Khumbu, Nepal and estimated radiative forcings. *Atmospheric Chemistry and Physics*, *14*(15), 8089–8103. https://doi.org/10.5194/acp-14-8089-2014

Lamare, M. L., Lee-Taylor, J., & King, M. D. (2016). The impact of atmospheric mineral aerosol deposition on the albedo of snow & sea ice: Are snow and sea ice optical properties more important than mineral aerosol optical properties? *Atmospheric Chemistry and Physics*, *16*(2), 843–860. https://doi.org/10.5194/acp-16-843-2016

Lau, W. K. M., Sang, J., Kim, M. K., Kim, K. M., Koster, R. D., & Yasunari, T. J. (2018). Impacts of snow darkening by deposition of light-absorbing aerosols on hydroclimate of Eurasia during boreal spring and summer. *Journal of Geophysical Research: Atmospheres*, *123*(16), 8441–8461. https://doi.org/10.1029/2018jd028557

Lehning, M., Bartelt, P., Brown, B., & Fierz, C. (2002). A physical SNOWPACK model for the Swiss avalanche warning: Part III: Meteorological forcing, thin layer formation and evaluation. *Cold Regions Science and Technology*, *35*(3), 169–184. https://doi.org/10.1016/s0165-232x(02)00072-1

Lehning, M., Bartelt, P., Brown, B., Fierz, C., & Satyawali, P. (2002). A physical SNOWPACK model for the Swiss avalanche warning: Part II. Snow microstructure. *Cold Regions Science and Technology*, *35*(3), 147–167. https://doi.org/10.1016/s0165-232x(02)00073-3

Lehning, M., Bartelt, P., Brown, B., Russi, T., Stockli, U., & Zimmerli, M. (1999). Snowpack model calculations for avalanche warning based upon a new network of weather and snow stations. *Cold Regions Science and Technology*, *30*(1–3), 145–157. https://doi.org/10.1016/s0165-232x(99)00022-1

Machulskaya, E. E., & Lykosov, V. N. (2008). An advanced snow parameterization for models of atmospheric circulation. *COSMO Newsletter*, *8*, 10–16.

Marmureanu, L., Marin, C. A., Andrei, S., Antonescu, B., Ene, D., Boldeanu, M., et al. (2019). Orange snow—A Saharan dust intrusion over Romania during winter conditions. *Remote Sensing*, *11*(21), 2466. https://doi.org/10.3390/rs11212466

Meinander, O., Kazadzis, S., Arola, A., Riihelä, A., Räisänen, P., Kivi, R., et al. (2013). Spectral albedo of seasonal snow during intensive melt period at Sodankylä, beyond the Arctic Circle. *Atmospheric Chemistry and Physics*, *13*(7), 3793–3810. https://doi.org/10.5194/acp-13-3793-2013

Mlawer, E. J., Taubman, S. J., Brown, P. D., Iacono, M. J., & Clough, S. A. (1997). Radiative transfer for inhomogeneous atmospheres: RRTM, a validated correlated-k model for the longwave. *Journal of Geophysical Research*, *102*(D14), 16663–16682. https://doi.org/10.1029/97jd00237

Monteiro, A., Basart, S., Kazadzis, S., Votsis, A., Gkikas, A., Vandenbussche, S., et al. (2022). Multi-sectoral impact assessment of an extreme African dust episode in the Eastern Mediterranean in March 2018. *Science of the Total Environment*, *843*, 156861. https://doi.org/10.1016/j.scitotenv.2022.156861

Nagorski, S. A., Kaspari, S. D., Hood, E., Fellman, J. B., & Skiles, S. M. (2019). Radiative forcing by dust and black carbon on the Juneau Icefield, Alaska. *Journal of Geophysical Research: Atmospheres*, *124*(7), 3943–3959. https://doi.org/10.1029/2018jd029411

Olson, M., & Rupper, S. (2019). Impacts of topographic shading on direct solar radiation for valley glaciers in complex topography. *The Cryosphere*, *13*(1), 29–40. https://doi.org/10.5194/tc-13-29-2019

Painter, T. H., Deems, J. S., Belnap, J., Hamlet, A. F., Landry, C. C., & Udall, B. (2010). Response of Colorado River runoff to dust radiative forcing in snow. *Proceedings of the National Academy of Sciences of the United States of America*, *107*(40), 17125–17130. https://doi.org/10.1073/pnas.0913139107

Peltoniemi, J. I., Gritsevich, M., Hakala, T., Dagsson-Waldhauserová, P., Arnalds, O., Anttila, K., et al. (2015). Soot on snow experiment: Bidirectional reflectance factor measurements of contaminated snow. *The Cryosphere*, *9*(6), 2323–2337. https://doi.org/10.5194/tc-9-2323-2015

Qian, Y., Gustafson, W. I., Leung, L. R., & Ghan, S. J. (2009). Effects of soot-induced snow albedo change on snowpack and hydrological cycle in western United States based on weather research and forecasting chemistry and regional climate simulations. *Journal of Geophysical Research*, *114*(D3), D03108. https://doi.org/10.1029/2008jd011039

Rahimi, S., Liu, X., Zhao, C., Lu, Z., & Lebo, Z. J. (2020). Examining the atmospheric radiative and snow-darkening effects of black carbon and dust across the Rocky Mountains of the United States using WRF-Chem. *Atmospheric Chemistry and Physics*, *20*(18), 10911–10935. https://doi.org/10.5194/acp-20-10911-2020

Rieger, D., Bangert, M., Bischoff-Gauss, I., Förstner, J., Lundgren, K., Reinert, D., et al. (2015). ICON–ART 1.0 – A new online-coupled model system from the global to regional scale. *Geoscientific Model Development*, *8*(6), 1659–1676. https://doi.org/10.5194/gmd-8-1659-2015

Rieger, D., Steiner, A., Bachmann, V., Gasch, P., Förstner, J., Deetz, K., et al. (2017). Impact of the 4 April 2014 Saharan dust outbreak on the photovoltaic power generation in Germany. *Atmospheric Chemistry and Physics*, *17*(21), 13391–13415. https://doi.org/10.5194/acp-17-13391-2017

Rohde, A. (2021). *The impact of the snow-darkening effect on snow cover and the atmosphere during a major dust event across Eurasia* (Doctoral dissertation). Karlsruhe Institute of Technologie (KIT). https://doi.org/10.5445/IR/1000141199

Rohde, A. (2023). ICON-ART data: Mineral dust on snow in Eurasia during a severe deposition event in March 2018 (ensemble mean values and statistics) [Dataset]. Karlsruhe Institute of Technology. https://doi.org/10.35097/1579

Sarangi, C., Qian, Y., Rittger, K., Bormann, K. J., Liu, Y., Wang, H., et al. (2019). Impact of light-absorbing particles on snow albedo darkening and associated radiative forcing over high-mountain Asia: High-resolution WRF-Chem modeling and new satellite observations. *Atmospheric Chemistry and Physics*, *19*(10), 7105–7128. https://doi.org/10.5194/acp-19-7105-2019

Sarangi, C., Qian, Y., Rittger, K., Ruby Leung, L., Chand, D., Bormann, K. J., & Painter, T. H. (2020). Dust dominates high-altitude snow darkening and melt over high-mountain Asia. *Nature Climate Change*, *10*(11), 1045–1051. https://doi.org/10.1038/s41558-020-00909-3

Schröter, J., Rieger, D., Stassen, C., Vogel, H., Weimer, M., Werchner, S., et al. (2018). ICON-ART 2.1: A flexible tracer framework and its application for composition studies in numerical weather forecasting and climate simulations. *Geoscientific Model Development*, *11*(10), 4043–4068. https://doi.org/10.5194/gmd-11-4043-2018

Shi, T., Cui, J., Chen, Y., Zhou, Y., Pu, W., Xu, X., et al. (2021). Enhanced light absorption and reduced snow albedo due to internally mixed mineral dust in grains of snow. *Atmospheric Chemistry and Physics*, *21*(8), 6035–6051. https://doi.org/10.5194/acp-21-6035-2021

Skiles, S. M., Flanner, M., Cook, J. M., Dumont, M., & Painter, T. H. (2018). Radiative forcing by light-absorbing particles in snow. *Nature Climate Change*, *8*(11), 964–971. https://doi.org/10.1038/s41558-018-0296-5

Skiles, S. M., & Painter, T. H. (2018). Assessment of radiative forcing by light-absorbing particles in snow from in situ observations with radiative transfer modeling. *Journal of Hydrometeorology*, *19*(8), 1397–1409. https://doi.org/10.1175/jhm-d-18-0072.1

Skiles, S. M., & Painter, T. H. (2019). Toward understanding direct absorption and grain size feedbacks by dust radiative forcing in snow with coupled snow physical and radiative transfer modeling. *Water Resources Research*, *55*(8), 7362–7378. https://doi.org/10.1029/2018wr024573

Skiles, S. M., Painter, T. H., Belnap, J., Reynolds, R. L., Goldstein, H. L., & Lin, J. (2015). Regional variability in dust-on-snow processes and impacts in the Upper Colorado River Basin. *Hydrological Processes*, *29*(26), 5397–5413. https://doi.org/10.1002/hyp.10569

Solomos, S., Kalivitis, N., Mihalopoulos, N., Amiridis, V., Kouvarakis, G., Gkikas, A., et al. (2018). From tropospheric folding to Khamsin and Foehn winds: How atmospheric dynamics advanced a record-breaking dust episode in Crete. *Atmosphere*, *9*(7), 240. https://doi.org/10.3390/atmos9070240

Svensson, J., Ström, J., Kivekäs, N., Dkhar, N. B., Tayal, S., Sharma, V. P., et al. (2018). Light-absorption of dust and elemental carbon in snow in the Indian Himalayas and the Finnish Arctic. *Atmospheric Measurement Techniques*, *11*(3), 1403–1416. https://doi.org/10.5194/amt-11-1403-2018

Svensson, J., Virkkula, A., Meinander, O., Kivekas, N., Hannula, H. R., Jarvinen, O., et al. (2016). Soot-doped natural snow and its albedo - Results from field experiments. *Boreal Environment Research*, *21*(5–6), 481–503.

Tuzet, F., Dumont, M., Arnaud, L., Voisin, D., Lamare, M., Larue, F., et al. (2019). Influence of light-absorbing particles on snow spectral irradiance profiles. *The Cryosphere*, *13*(8), 2169–2187. https://doi.org/10.5194/tc-13-2169-2019

Tuzet, F., Dumont, M., Lafaysse, M., Picard, G., Arnaud, L., Voisin, D., et al. (2017). A multilayer physically based snowpack model simulating direct and indirect radiative impacts of light-absorbing impurities in snow. *The Cryosphere*, *11*(6), 2633–2653. https://doi.org/10.5194/tc-11-2633-2017

Usha, K. H., Nair, V. S., & Babu, S. S. (2020). Modeling of aerosol induced snow albedo feedbacks over the Himalayas and its implications on regional climate. *Climate Dynamics*, *54*(9–10), 4191–4210. https://doi.org/10.1007/s00382-020-05222-5

Vionnet, V., Brun, E., Morin, S., Boone, A., Faroux, S., Le Moigne, P., et al. (2012). The detailed snowpack scheme Crocus and its implementation in SURFEX v7.2. *Geoscientific Model Development*, *5*(3), 773–791. https://doi.org/10.5194/gmd-5-773-2012

Vogel, B., Hoose, C., Vogel, H., & Kottmeier, C. (2006). A model of dust transport applied to the Dead Sea area. *Meteorologische Zeitschrift*, *15*(6), 611–624. https://doi.org/10.1127/0941-2948/2006/0168

Warren, S. G., & Brandt, R. E. (2008). Optical constants of ice from the ultraviolet to the microwave: A revised compilation. *Journal of Geophysical Research*, *113*(D14), D14220. https://doi.org/10.1029/2007jd009744

Warren, S. G., & Wiscombe, W. J. (1980). A model for the spectral albedo of snow. II: Snow containing atmospheric aerosols. *Journal of the Atmospheric Sciences*, *37*(12), 2734–2745. https://doi.org/10.1175/1520-0469(1980)037<2734:amftsa>2.0.co;2

Wilcoxon, F. (1945). Individual comparisons by ranking methods. *Biometrics Bulletin*, *1*(6), 80–83. https://doi.org/10.2307/3001968

Wilks, D. S. (2016). "The stippling shows statistically significant grid points": How research results are routinely overstated and overinterpreted, and what to do about it. *Bulletin of the American Meteorological Society*, *97*(12), 2263–2273. https://doi.org/10.1175/bams-d-15-00267.1

Winker, D. M., Hunt, W. H., & Hostetler, C. (2004). Status and performance of the CALIOP lidar. *Proceedings of SPIE - The International Society for Optical Engineering*, *5575*, 8–15.

Winker, D. M., Hunt, W. H., & McGill, M. J. (2007). Initial performance assessment of CALIOP. *Geophysical Research Letters*, *34*(19), L19803. https://doi.org/10.1029/2007gl030135

Wiscombe, W. J., & Warren, S. G. (1980). A model for the spectral albedo of snow. I: Pure snow. *Journal of the Atmospheric Sciences*, *37*(12), 2712–2733. https://doi.org/10.1175/1520-0469(1980)037<2712:amftsa>2.0.co;2

WMO Barcelona Dust Regional Center. (2021). WMO sand and dust storms warning advisory and assessment system. Retrieved from https://dust.aemet.es/

Yasunari, T. J., Koster, R. D., Lau, W. K. M., & Kim, K.-M. (2015). Impact of snow darkening via dust, black carbon, and organic carbon on boreal spring climate in the Earth system. *Journal of Geophysical Research: Atmospheres*, *120*(11), 5485–5503. https://doi.org/10.1002/2014jd022977

Zängl, G., Reinert, D., Rípodas, P., & Baldauf, M. (2015). The ICON (ICOsahedral Non-hydrostatic) modelling framework of DWD and MPI-M: Description of the non-hydrostatic dynamical core. *Quarterly Journal of the Royal Meteorological Society*, *141*(687), 563–579. https://doi.org/10.1002/qj.2378

Zsoter, E., Arduini, G., Prudhomme, C., Stephens, E., & Cloke, H. (2022). Hydrological impact of the new ECMWF multi-layer snow scheme. *Atmosphere*, *13*(5), 727. https://doi.org/10.3390/atmos13050727